Electrochemical synthesis of nanowire anodes from spent lithium ion batteries

Pier Giorgio Schiavi [a, *], Luca Farina [a, b], Robertino Zanoni [a], Pietro Altimari [a], Iulia Cojocariu [a, c], Antonio Rubino [a], Maria Assunta Navarra [a], Stefania Panero [a], Francesca Pagnanelli [a]

[a] Dipartimento di Chimica, Università La Sapienza, Piazzale Aldo Moro 5, 00185, Rome, Italy
[b] ENEA, FSN Department, Via E. Fermi 45, 00044, Frascati, RM, Italy
[c] Peter Grünberg Institute (PGI-6), Forschungszentrum Jülich GmbH, 52425, Jülich, Germany

A B S T R A C T

A novel process is proposed to produce nanostructured batteries anodes from spent lithium-ion batteries. The electrodic powder recovered by the mechanical treatment of spent batteries was leached and the dissolved metals were precipitated as cobalt carbonates. Two different precipitation routes were separately tested producing cobalt carbonates with different Cu and Fe contents. Nanowire anodes were produced by electrodeposition into nanoporous alumina templates from the electrolytic baths prepared by dissolution of the precipitated carbonates. The electrochemical performances of the produced anodes were evaluated as compared to nanowire anodes produced with the same electrodeposition method but using a synthetic cobalt bath. The application of the carbonates produced by directly precipitating all the leached metals gave nanowires with capacity about halved as compared to the nanowires electrodeposited from the synthetic bath. Selectively removing Cu and Fe prior cobalt carbonate precipitation yielded, in contrast, nanowires with capacity initially larger and then gradually approaching that attained by the nanowire electrodeposited from the synthetic bath. A detailed analysis is presented describing the role of metallic impurities in determining the capacity of the produced nanowires. The impact of the illustrated results for the development of sustainable recycling processes of lithium-ion batteries is discussed.

1. Introduction

The application of batteries has been steadily increasing over the past two decades mainly driven by the growing market of consumer electronics. In accordance with statistics, the global batteries market has increased by 800% between 2000 and 2010 and accounted for $54 billion (U.S.) in 2013 [1]. In this framework, lithium ion batteries (LIBs) have attracted increasing attention owing to their high energy and power density, long cycle life and low self-discharge [2,3], arriving to cover currently the largest share of the batteries market. A further huge growth in the production of LIBs is expected during the following few years stimulated by the transition to clean electric transportation. This transition is predicted to drive the global LIBs market to $32 billion by 2020. This will dramatically increase the volume of spent LIBs, which is estimated to reach 500 thousand tons by 2020.

The recycling of spent LIBs becomes then fundamental to prevent the dispersion into the environment of hazardous elements, which may result from inappropriate dismissal practices, but particularly to sustain the demand of the materials needed to produce new LIBs. Particularly, batteries electrodes materials including strategic or critical raw materials such as graphite, cobalt, nickel and manganese, which account for more than 50% of the battery cost [4], need to be recovered and recycled into the batteries manufacturing chain. Recycled battery materials such as cobalt, nickel and manganese can be found in new batteries already today. Hydrometallurgical processes can be implemented ensuring the complete recovery of the different electrodic materials into separate streams. Major bottleneck reducing the economic and environmental sustainability of hydrometallurgical processes is

represented by the numerous and costly stages performed to separate the different electrode materials. These numerous process stages are mainly motivated by the complex chemistry of the batteries cathodes. Originally, these were mainly composed of $LiCoO_2$, but, more recently, in order to reduce the batteries cost, cobalt has been partially substituted with nickel and manganese, which has driven the development of new cathode materials including, for example, $LiNiO_2$, $LiNi_xMn_zCo_yO_2$, $LiNi_xCo_yAl_zO_2$ and $LiMn_2O_4$ [5−8]. Cobalt, nickel and manganese exhibit extremely similar physical-chemical properties and can be separated only by lengthy and complex separation-purification stages, including leaching, precipitation, solvent extraction, stripping, electrowinning. These impose large solvents consumption, the generation of large wastes volumes, and elevate capital expenditures, which contribute to compromising the economic and environmental sustainability of hydrometallurgical recycling processes.

An effective strategy overcoming these limitations is the intensification of hydrometallurgical processes by the integrated recycling and production of electrodic batteries materials. The main idea is that the different electrodic materials do not need to be separated from any other if they are used to produce new batteries electrodes. In this latter case, the solution obtained by leaching the electrodic powder of spent LIBs can be directly used to "resynthesize" new batteries electrodes, thus excluding the downstream costly and complex separation of the different metals.

Different methods have been recently implemented to "resynthesize" cathode and anode materials from the leaching solution generated by the hydrometallurgical treatment of spent LIBs. Wang and co-workers [9−11] produced a mixed $LiNi_xMn_yCo_zO_2$ by co-precipitation of nickel, manganese and cobalt from the purified leaching solution. A similar process was proposed by Weng et al. [12], whereby a separation stage was introduced to remove magnesium impurities, which could negatively influence the electrochemical performances of the produced electrode material. A sol-gel synthesis method was implemented following leaching with malic acid by Yao et al. [13] to produce the cathode material $LiNi_xMn_yCo_zO_2$. A more convolute process including the combination of co-precipitation, hydrothermal and calcination processes was performed by Li et al. [14] to produce a lithium-rich layered cathode oxide $Li_{1.2}Co_{0.13}Ni_{0.13}Mn_{0.54}O_2$.

Recently, increasing attention has been devoted to the application of transition metal oxides to produce conversion reaction-based anodes of LIBs [15−17]. These anodes can ensure capacity (~1000 mAh/g) significantly larger as compared to the graphite anodes (~350 mAh/g) currently employed in LIBs [15]. Motivated by this result, the direct synthesis of transition metal oxides anodes from spent LIBs has been investigated. Spray pyrolysis was implemented to synthesize nanocomposite $Ni_{0.8}Co_{0.1}Mn_{0.1}O_{1.1}$ porous microspheres, which exhibited excellent specific capacity (1180 mAh/g) when employed as anode material in LIBs [18]. Hu et al. [19] produced Co_3O_4 nanoparticles by hydrometallurgical treatment of the electrodic powder recovered from spent LIBs and sol-gel synthesis. On the other hand, transition metal oxides anodes are characterized by large volume changes between charge and discharge cycles, which causes cycle fading and thus hinder the application in LIBs. This issue can be solved by the application of transition metal oxides nanostructures. The application of metal oxides nanostructures with purposefully tailored morphology can decrease the strain determined by the volume changes, thus enhancing the rate capability, and it can increase the specific surface contact between the electrolyte and the anode. For this purpose, the application of one-dimensional nanostructures including nanowires and nanotubes has been proven to configure a competitive technological solution.

Therefore, in order to directly produce high-performance and low-cost conversion reaction-based anodes from spent LIBs, strategies allowing for the morphology controlled synthesis of transition metal oxides nanostructures must be integrated into the recycling chain. With bulk synthesis methods, including, for example, sol-gel synthesis and co-precipitation [19], and with spray pyrolysis [18], it is difficult to effectively control the electrode material morphology, which ultimately determines the attained electrochemical performances.

In this article, we apply the electrodeposition technique to directly synthesize nanowire anodes from spent LIBs. The proposed route relies on the implementation of an electrodeposition method previously developed by the authors to synthesize cobalt nanowires from cobalt sulphate solutions [20]. With this method, an array of metal nanowires standing over a thin current collector plate can be produced by electrodeposition into the nanopores of anodized alumina templates and successive selective dissolution of alumina. As compared to alternative nanowires strategies as, for example, hydrothermal synthesis, this method allows effectively controlling the nanowires length distribution and can ensure, at the same time, direct formation of a metallic core covered by a thin metal oxide layer. This can enhance the electronic conductivity and prevent the application of conductive binders.

In order to evaluate the potential to implement the proposed process at industrial scale, the electrodic powder recovered by industrial scale granulation and sieving of spent LIBs was used. This introduces impurities into the process which could dramatically influence the electrochemical performances of the produced nanowires; typically such impurities have been excluded by previous studies through the lab-scale sorting of batteries and the manual separation of the electrodic powder.

Overall, a recycling process is here proposed whereby the electrodic powder is leached by sulphuric acid, and the dissolved metals are successively precipitated as carbonates. These carbonates are then used to prepare the electrolytic bath needed to perform the nanowires electrodeposition. The impact of impurities on the electrochemical performances of the produced electrode material is evaluated. To this purpose, the following two different process routes are evaluated: (i) directly precipitating all the leached metals, including copper and iron impurities, to produce a low-purity carbonate, (ii) selectively precipitating copper and iron impurities and then precipitating the remaining metals to produce a partially purified metal carbonates. The anodes produced from the separated carbonates are benchmarked against the cobalt nanowire anodes produced by implementing the same electrodeposition method with the electrolytic solution prepared by using high-purity cobalt salt.

2. Materials and methods

2.1. Recovery process − electrolytic baths

A scheme of the implemented recycling process is reported in Fig. 1. Exhausted LIBs were collected, granulated and sieved by an Italian waste disposal company (SEVal s.r.l.). Following granulation (Fig. 1-1), a sample of 50 kg was sieved by using a vibrating sieve (Fig. 1-2) with a grid's mesh size of 0.5 mm, which allowed separating the electrodic powder. Metal extraction was performed by leaching (Fig. 1-3) 200 g of electrodic powder using sulphuric acid and hydrogen peroxide as oxidant and reducing agent, respectively, allowing attaining a metals extraction yield up to 96% [21]. Electrodic powder was leached with H_2SO_4 1.3 M in a jacketed glass reactor at controlled temperature of 85 °C. A solid to liquid ratio of 1:10 was employed and the leaching was carried out under stirring for 3 h. Following leaching, a filtration was performed to separate the residual carbon fraction. The extracted metals were then
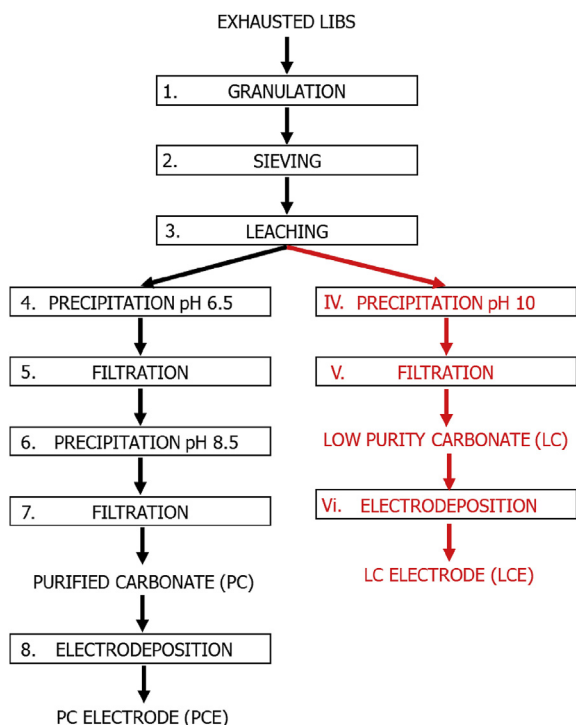
Fig. 1. Scheme of the proposed synthesis processes.

recovered by following a one-step or a two-steps precipitation routes. With the two-steps precipitation route (Fig. 1, left branch), the pH of the filtrated solution was initially raised to and maintained at pH 6.5 by using NaOH 6 M to selectively precipitate copper and iron (Fig. 1-4). After filtration (Fig. 1-5), Na_2CO_3 was added to the purified solution until reaching pH 8.5 (Fig. 1-6). A purified carbonate (PC) was thus precipitated and then filtered (Fig. 1-7). With the one-step precipitation route (Fig. 1, right branch), the selective precipitation of copper and iron was discarded and all the extracted metals were simultaneously precipitated. To this purpose, Na_2CO_3 was added to the solution until pH 10 was reached, which led to the precipitation of low purity carbonates (LC). As compared to the two-steps precipitation route, the one-step precipitation considerably simplifies the recycling process by decreasing the number of process stages, and it can increase the recovery yield of cobalt by excluding the partial precipitation of cobalt taking place during the selective separation of copper and iron at pH 6.5. The recovered metal carbonates were washed with distilled water until the Na^+ concentration was lower than 200 mgL^{-1}. The electrolytic baths were then obtained by dissolving the carbonates in the smallest amount of H_2SO_4 and adding 1 mL of H_2O_2. These concentrated solutions were diluted to a volume of 50 mL with distilled water, and 50 gL^{-1} of H_3BO_3 were added to any electrolytic bath. The content of any metal in the electrolytic solutions was measured by atomic absorption spectroscopy (AAS — Analytic Jena ContrAA300).

2.2. Synthesis of nanowires-based electrodes

The anodes were synthesized by a template electrodeposition method recently proposed by the authors [20,22]. Nanowires were synthesized by electrodeposition into the nanopores of an alumina template generated by a one-step anodization of low-purity aluminium. Electrodeposition was performed in a magnetically stirred three-electrode jacketed glass cell at constant temperature of $35 \pm 0.2\,°C$. A 25×20 mm Pt gauze, Ag/AgCl saturated electrode and anodic alumina with exposed area of 1.3 cm^2 were used as counter, reference and working electrode, respectively. The electrolytes employed to perform the electrodeposition were obtained by dissolving purified carbonates or low purity carbonates. The electrodes produced from purified or low-purity carbonate solutions will be denoted throughout the article as PC and LC electrodes (PCE and LCE), respectively. The electrodeposition was performed by applying a constant voltage signal of −8 V vs Ag/AgCl for 50 ms and then the current was kept at zero for 2000 ms. These two pulses were cycled until 2/3 of the alumina nanopores length was filled by the electrodeposited metals. The as obtained electrode was employed as working electrode to perform the sub-sequent copper electrodeposition. The same electrochemical configuration adopted for the electrodeposition of metals from the carbonates solutions was used for Cu electrodeposition, but a copper plate was used as counter electrode. Copper electrodeposition was carried out until a copper thin film uniformly covered the external surface of the alumina template. This allowed forming a copper current collector composed by copper nanowires connected to a thin copper plate. Finally, alumina and aluminium were completely removed by selective etching in NaOH 6 M. This left an array of free standing cobalt nanowires connected to the copper current collector. The obtained electrodes were punched to obtain disks with geometrical surface area of 0.5 cm^2.

2.3. Electrochemical measurements

Cyclic voltammetry (CV) and electrochemical impedance spectroscopy (EIS) were performed by using a three-electrode polypropylene T-cell, with the produced electrodes employed as working electrode, and two lithium disks employed as counter and reference electrode. Two Whatman glass fiber membranes were used to separate the anodic and the cathodic side. Commercial 1 M $LiPF_6$ in 1:1 v/v ethylene carbonate: dimethyl carbonate solution (Solvionic) was used as electrolyte. Each cell was assembled in an argon-filled glove box with a content of O_2 and H_2O less than 1 ppm. CV was run with a scan rate of 0.2 mVs^{-1} over the 0.01−3 V vs Li^+/Li voltage range. EIS was performed in the 200 kHz−10 Hz frequency range, using 10 mV amplitude AC pulses. CV and EIS were carried out using VSP BioLogic instrument. Galvanostatic tests were performed using Maccor Series 4000 Battery Test System in a two-electrode cell configuration, under a charge/discharge current density of 2 Ag^{-1} (referred to the amount of CoO in SBE).

2.4. Electrodes characterization

Field emission scanning electron microscopy (SEM, Zeiss Auriga) was employed to characterize the morphology and size of electrodes. Focused ion beam (FIB, Orsay Physics - Cobra Ga column) was used to generate electrode cross sections. The chemical composition of the electrodes was determined by energy dispersive X-ray spectroscopy (EDX, Bruker QUANTAX 123 eV). X-ray photoelectron spectra were obtained using a modified Omicron Nano-Technology MXPS system. The spectra were excited by monochromatic Al kα or achromatic Al Kα and Mg Kα photons (hν = 1486.7, 1486.6 and 1253.6 eV, respectively), generated operating the anode at 14−15 kV, 10−20 mA. Use of different photons was necessary in order to overcome interference of photoemission and Auger signals, whenever possible, and to enhance resolution. Experimental spectra were theoretically reconstructed by fitting the peaks to symmetric Voigt functions and the background to a Shirley or a linear function. XPS atomic ratios (±10% associated error) were obtained from experimentally determined area ratios, corrected for the corresponding theoretical cross sections and for a

square root dependence of the photoelectrons kinetic energies. All the samples were mounted on amagnetic stainless steel tips with a conductive adhesive tape, and the upper surface of the holder was covered with Teflon tape to mask lines from the tips which could have been detected because of the small diameter of each sample. Peak assignments were given by reference to previous literature reports [23].

3. Results and discussion

3.1. Electrolytic baths and electrodes characterization

The granulated spent LIBs were separated into two fractions by sieving. The fraction below 0.5 mm was mainly composed of graphite, carbon and cathodic material, while the fraction above 0.5 mm contained plastics, metallic case fragments, copper and aluminium coming from the current collectors (Fig. S1 of Supporting Information). The fraction below 0.5 mm was leached and the leach liquor composition is reported in Table 1. Cobalt was the predominant metal contained in the electrodic powder. This result can be explained by observing that $LiCoO_2$ was the cathode material employed in first generation LIBs, with $LiCoO_2$ covering about the 40% of produced LIBs [6,9]. Surprisingly, relevant amounts of Cd and Zn were found in the leach liquor (Table 1). Cd and Zn are not employed to produce LIBs, and their presence in the leach liquor should be here imputed to the contamination of the processed LIBs feedstock with different types of batteries. This contamination typically occurs at industrial scale owing to the inefficiencies of the currently implemented batteries sorting methods, which largely rely on manual operation. The obtained leach liquor was processed by following the two routes reported in Fig. 1. PC and LC carbonates were characterized (Table S1, Supporting Information) and employed as raw materials for the production of the electrolyte baths. Table 1 reports the composition of the electrolytic baths obtained from low purity carbonate (LC), purified carbonate (PC) and synthetic cobalt salt (SB). These data demonstrate that the precipitation at pH 6.5 could selectively remove iron, thus decreasing the copper concentration in the electrolytic bath prepared with the PC carbonate by 20 times, as compared to the application of LC carbonate. Any other metal (Co, Ni, Mn, Cd) exhibited very similar concentration in the two electrolytic solutions prepared with the LC and the PC carbonate, respectively. We remark that further purification/separation of the metals would require to introduce complex and costly process stages, including for example, solvent extraction. While this would allow to recover the metals as high purity grade salts [21], it would considerably increase the capital and operating process expenditures, compromising the sustainability of the recycling process. For this reason, the low purity LC and PC carbonates were used, without further purifications, as raw materials for the synthesis of nanowires electrodes by electrodeposition. Fig. 2 shows SEM images of the produced electrodes. A compact and ordered array of nanowires with narrow length distribution was obtained for any produced electrode. Average nanowires length and diameter were around 4 µm and 50 nm, respectively. The nanowires portion composed of the metals electrodeposited from the PC and LC carbonates

solutions extends from the top to about 1/3 of the nanowire length while the copper nanowires current collector covers the remaining length (Fig. 2E). The same structure was obtained for both PCE and LCE but, as it is apparent from enlarged cross sectional images (Fig. 2C–D), the electrodes obtained by electrodeposition from the PC carbonate solution are characterized by nanoflakes covering the nanowires surface. The appearance of nanoflakes can be imputed to the precipitation of cobalt hydroxide. The reduction of water and protons taking place along with the electrochemical reduction of metals at the working electrode surface increases the local pH and thus enables the precipitation of cobalt hydroxide, provided that the concentrations of Co^{2+} and OH^- are sufficiently high [24]. However, unlike the PCE electrode, the SEM images of the LCE electrode do not evidence the presence of nanoflakes covering the nanowires surface. The absence of cobalt hydroxide nanoflakes over the LCE electrode can be attributed to different mechanisms. Firstly, the amount of copper that is electrodeposited along with cobalt during the synthesis of the LCE electrode is much larger as compared to the synthesis of the PCE electrode. Therefore, even after the pH triggering cobalt hydroxide precipitation is attained, the growth of the cobalt hydroxide nanoflakes over the LCE electrode can be masked by the concurrent electrodeposition of metallic copper. This effect can be negligible during the synthesis of the LCE electrode owing to the lower partial copper electrodeposition current. Moreover, cobalt and cobalt alloys can catalyse proton and water reduction much better than copper [25]. LCE electrode was mainly composed of copper (Tables 2 and 3). This may decrease the water reduction rate and thus prevent or slow down the pH increase required to sustain cobalt hydroxide precipitation.

EDX and XPS analysis were performed to characterize the bulk and the surface composition of the nanowires, respectively. Table 2 reports the atomic compositions derived by EDX of PCE and LCE electrodes. For comparison, the atomic composition analysis of the SBE electrode produced by electrodeposition from a synthetic cobalt solution is included in Table 2. EDX results (Table 2) reveal significant differences between the LCE and PCE electrodes, with the LCE electrodes characterized by a 4 times larger copper atomic fraction and significantly lower cobalt and oxygen atomic fractions. Particularly, the cobalt atomic fraction is about halved in LCE electrodes as compared to the PCE electrodes.

In order to explain the larger copper content in LCE electrode, we notice that copper is the most noble metal in the LC electrodeposition bath (Table 1) and is thus characterized by the lowest cathodic reduction potential. Accordingly, while the cathodic potential is, during electrodeposition, large enough to sustain the electrochemical reduction of all the metals in the solution, the electrochemical reduction of copper proceeds with the largest overpotential, which increases the copper reduction rate as compared to the other metals. This can in turn increase the faradaic efficiency of copper leading to the synthesis of a copper rich electrode.

In Fig. 3A, the XPS survey scan of the two electrodes are reported. The relative atomic ratios among main peaks are reported in Table 3. Several metal peaks were detected, owing to the heterogeneity of the PCE and the LCE electrodes. The intense F 1s and F

Table 1
Composition of the leach liquor and of the electrolytic baths [gL^{-1}] obtained from low purity carbonate (LC), purified carbonate (PC) and synthetic cobalt salt (SB).

Solution	Co	Ni	Mn	Cu	Fe	Cd	Zn	Al	Li
Leach liquor	19.6±1.9	4.7±0.6	3.3±0.9	0.9±0.1	0.6±0.1	0.5±0.01	0.4±0.05	1.1±0.1	3.2±0.1
PC	45.9	13.4	11.8	0.1	0.01	1.2	0.9	-	-
LC	47.7	14.3	9	2.2	1.2	1.1	0.9	-	-
SB	50	-	-	-	-	-	-	-	-
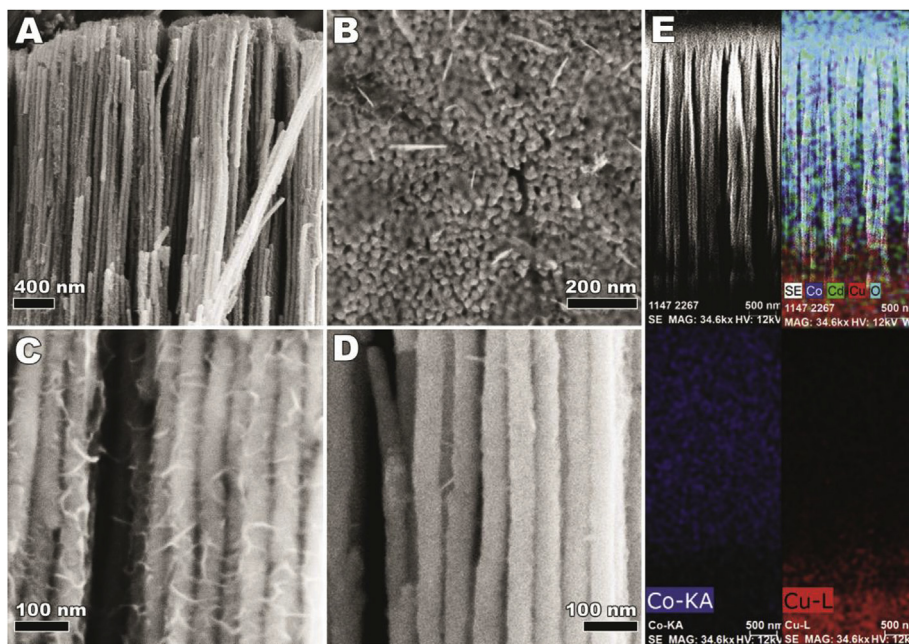
Fig. 2. Cross sectional (A) and top-view (B) SEM images of PCE. Cross sectional enlarges of PCE (C) and LCE (D). E) EDX mapping after cross sectional FIB milling of PCE.

Table 2
Electrodes composition [at.%] obtained from EDX analysis.

Electrode	Co	Ni	Cd	Mn	Cu	Zn	Fe	O
PCE	47.1	1.3	2.5	1.3	11.6	2.0	1.8	32.3
LCE	22.2	4.3	2.5	-	42.7	-	2.4	25.8
SBE	77.3	-	-	-	-	-	-	22.7

Table 3
Relative atomic ratios obtained from XPS and EDX analyses.

Electrode	analysis	Co/Cu	Co/Cd	Co/Ni
PCE	XPS	3.5	11	14
	EDX	4.0	18.4	36.2
LCE	XPS	1.3	39	5.7
	EDX	0.5	8.8	5.2

Auger peaks, as well as the $(-CF_2-)_n$-related component of the C 1s peak at 292 eV, are due to Teflon tape used for mounting of the

sample (see Experimental Section). Apart from the prevailing contributions of Co (2p, 3p and 3s) and Cu (2p, 3p and 3s) states, also Cd 3d, Zn 2p and Ni 2p peaks can be traced from inspection of Fig. 3 for the LCE electrode, while the PCE electrode presents those same elements plus Si (2p and 2s), coming from the aluminium template. Notice that the contemporary presence of Co and Cu as the major components hampers an identification of Mn through its most intense peak, Mn 2p, because of the overlapping of the corresponding ionization region with the sequence of either Co LMM Auger excited by Mg Kα photons or Cu $L_3M_{2,3}M_{4,5}$ Auger lines, when Al Kα photons are employed. As for the relative assignments, Cu 2p is a complex peak in LCE and PCE, and it shows, after curve fitting, the coexistence of Cu(I) and Cu(II) oxides. As shown in Table 3, the trend in relative atomic ratios of Co vs. Cu, Cd and Ni shows variations with respect of the bulk analysis afforded by EDX. Only in the case of Co/Ni, a close comparison can be made among the XPS and EDX ratios (14 vs. 9.53; 5.7 vs. 5.2, respectively for PCE and LCE), which calls for a nearly homogeneous in-depth distribution of Ni in LCE and a moderate surface enrichment in PCE. In the other two
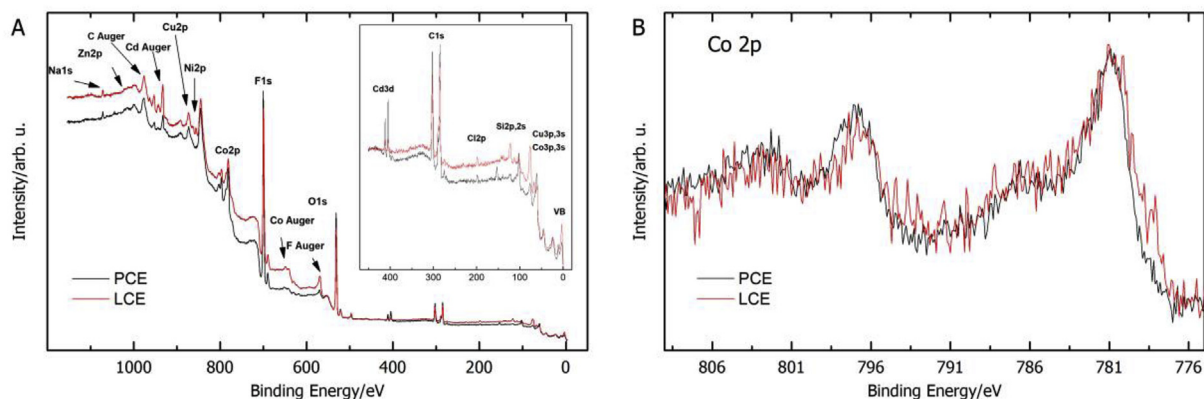
Fig. 3. A) Wide range photoemission spectra of PCE and LCE with relative assignments, taken with Mg kα achromat. B) Co 2p3/2,1/2 photoemission regions of PCE and LCE taken with Al kα monochromatic radiation.

cases, the Co/Cd and Co/Cu ratios indicate an opposite behaviour of PCE and LCE, the former experiencing a relative surface depletion of cobalt, and the latter an enrichment. The combination of Cd 3d$_{5/2}$ BE and Cd Auger M$_4$N$_{4,5}$N$_{4,5}$ kinetic energy results in a value of 785.6 eV for Cd modified Auger parameter, α', which reveals the presence of CdO and/or Cd(OH)$_2$. Based on the binding energy and the lineshape of Ni 2p peaks, these peaks are assigned to Ni(OH)$_2$ with the possible presence of a minor quantity of NiO. In order to further investigate the cobalt oxidation state, Co 2p spectra of the two samples are reported in Fig. 3B. Their lineshape reveal the presence of Co(II) oxide in both PCE and LCE samples, with binding energy values of 780.8 and 780.6, respectively, which closely compare with literature reports (780.4). An additional component results only for LCE at 778.5 eV and can be assigned to Co(0) [26].

3.2. Electrochemical evaluation

The produced electrodes were employed as working electrodes in a half-lithium cell. Fig. 4A displays the evolution of the current versus potential attained during the second cycle of the cyclic voltammetry performed by scanning the potential over the range 0.01−3.0 V with rate equal to 0.2 mVs^{-1}. The cyclic voltammogram of the LCE electrode is qualitatively similar to that obtained with the SBE electrode where CoO is the only electroactive material. Particularly, cathodic and anodic peaks are detected for the two electrodes at nearly identical potential values. This indicates that the lithium storage follows the same mechanism in the SBE and LCE electrodes. Particularly, the cathodic peak at about 1.7 V can be ascribed to the reduction of CoO and to the formation of Li$_2$O, while the peak at 2.1 V during the anodic scan is determined by the oxidation of cobalt to CoO and by the Li$^+$ extraction [27−30]. The other faradaic peaks on the cyclic voltammograms can be ascribed to the reversible electrochemically driven polymerization originated by electrolyte reduction over the low potential range [29,31,32].

The cathodic and anodic peaks determined by CoO reduction/ formation and by the reversible electrolyte polymerization were also found for PCE (Fig. 4A). However, a significant increase in the current associated to these peaks was observed with PCE. This can be attributed to the larger amount of CoO contained in PCE. By combining EDX (Table 2) and XPS (Table 3) analyses, it can be indeed derived that the cobalt amount in PCE is larger than in LCE (Table 2), and that, in accordance with the Co 2p results, cobalt is almost completely present as CoO at the surface of PCE (Fig. 3B). Further, XPS analysis reveals that LCE is characterized by a relevant metallic cobalt component (Fig. 3B), with a significantly lower CoO component on the nanowires surface, as compared to PCE. The lowest amount of cobalt was attained, in accordance with EDX analysis, with LCE.

Further cathodic peaks, undetected with LCE and SBE electrodes, appeared in the cyclic voltammogram of the PCE electrode, which can be attributed to the impurities. Particularly, a cathodic peak close to the reversible electrolyte reduction was detected at 0.7 V followed by another cathodic peak at 0.3 V. The cathodic peak at 0.7 V could be ascribed to Cd-Li alloying, which can occur after CdO reduction according to the following reaction scheme [33]:

$$CdO + 2Li \leftrightarrows Cd + Li_2O \tag{1}$$

$$Cd + 3Li \leftrightarrows Li_3Cd \tag{2}$$
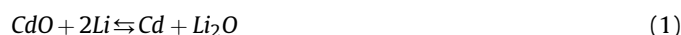
Reactions Eq. (1) and Eq. (2) contribute to the transferred charge with a specific capacity contribution equal to 418 mAhg^{-1} and 628 mAhg^{-1}, respectively. We notice that Zn-Li alloying might also take place over the same potential range following ZnO reduction [34]. The cathodic peak at 0.3 V could be attributed to the reduction of manganese oxide to metallic manganese and the formation of Li$_2$O [35]. In order to explain why the contributions of Cd and Mn could be detected with the PCE electrode while they were absent with the LCE electrode, we remark that, according to the XPS analysis, PCE electrodes were characterized by a CdO surface enrichment when
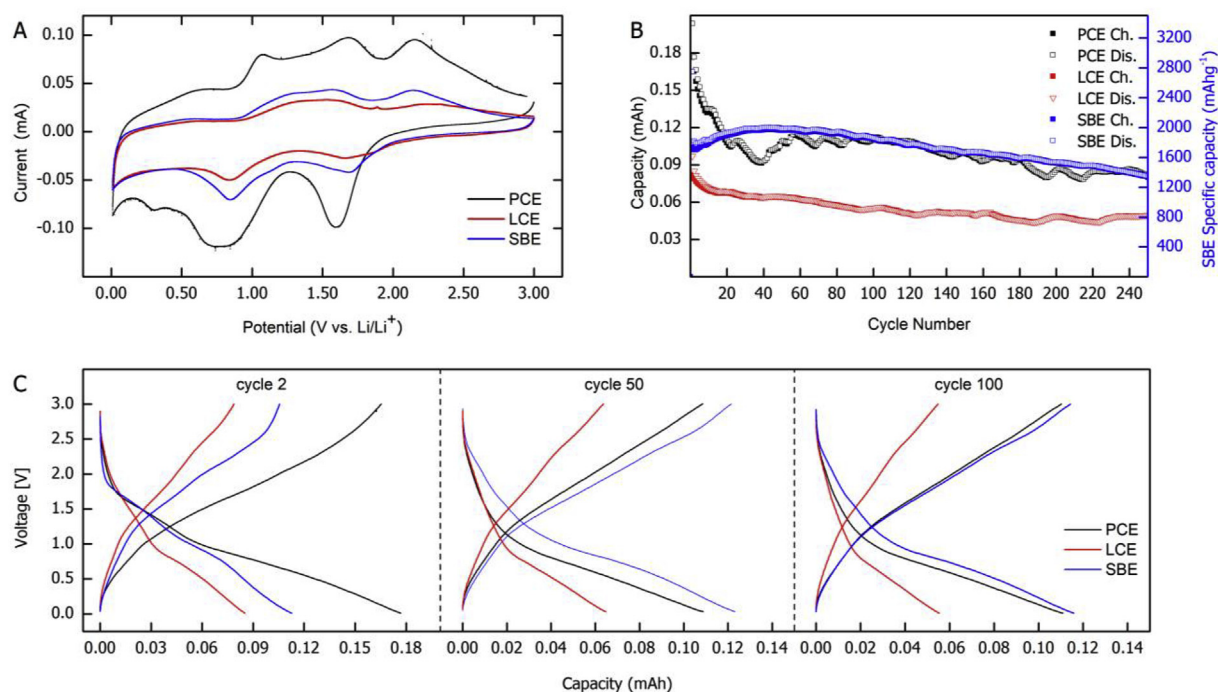
Fig. 4. A) Cyclic voltammograms recorded within 0.01−3 V at 0.2 mVs^{-1}. B) Cycling performance at 2 A g^{-1} (referred to the amount of CoO in SBE). C) Charge-discharge curves of cycles: 2, 50, 100.

compared with LCE electrodes (Table 3), and that Mn could not be detected by EDX analysis of the LCE electrode (Table 2).

All the voltammetric cycles recorded for the different electrodes are reported in Fig. S2. Overall, the current peaks and the reaction potential values no longer varied during the experiment starting from the second cycle, providing an indication of reaction reversibility. Additional peaks detected at the first cycle can be attributed to the expected electrolyte decomposition.

The electrochemical performance of produced electrodes was evaluated by galvanostatic charge-discharge cycling. Galvanostatic charge/discharge capacity and voltage profiles are reported in Fig. 4B and C, respectively. For comparison, the galvanostatic charge-discharge curves obtained at the same current with the SBE electrode, which was characterized in our previous work [20], is included. The analysis of the SBE electrode is here intended to quantify the electrochemical performance that could be obtained by using a high-purity cobalt salt during the electrodes synthesis. Accordingly, evaluating the electrochemical performances of the PCE and LCE electrodes as compared to the SBE electrode can provide a direct indication about the advantage to introduce additional stages into the proposed recycling process (Fig. 2) allowing further purifying/separating the metals recovered from spent LIBs.

At this point, it is worth to notice that the approach most commonly followed to quantify the specific capacity of the electrode is to divide the electrode capacity by the mass of the electroactive species, which are here represented by the metal oxides covering the metallic nanowire core [20,36,37]. However, specific capacity normalized by the mass of the electroactive species could be reported only for the SBE electrode (Fig. 4B blue axis), where CoO is the only electroactive material and could be accurately quantified. Differently, in the PCE and LCE electrodes, multiple metals oxides were found, making it difficult the estimation of the electroactive material loading and thus excluding the evaluation of the specific capacity. For this reason, the performances of the PCE, LCE and SBE were compared in terms of the electrode capacity (Fig. 4B, left axis). Particularly, we compared the evolutions of the electrodes capacities attained during galvanostatic charge/discharge cycles conducted at a current density of $2 Ag^{-1}$, referred to the mass of CoO in the SBE. We emphasize that this comparison is here justified by considering that all the electrodes have identical geometric area and are composed of nanowires with identical length, number density and diameter. The derivation of the specific capacity normalized by the total mass of nanowires including the oxide layer and the metallic core minus the mass of the copper current collector was reported in the Supporting Information for the PCE electrode.

The LCE electrode exhibits capacity always lower as compared to the PCE and SBE electrodes (Fig. 4B). This is in agreement with the reduced current densities detected by the cyclic voltammogram of the LCE electrode. The lower capacity can be ascribed to the larger copper amount found in LCE (Table 2). Taking constant the electrodeposition template volume, an increased copper fraction reduces the cobalt loading, which determines a lower capacity with respect to the SBE and PCE. As demonstrated in our recent work [20], copper nanowires synthesized with the implemented electrodeposition method cannot provide a significant faradaic contribution to the total recorded capacity.

In agreement with the analysis of the cyclic voltammograms (Fig. 4A), during the initial charge/discharge cycles, the PCE electrode exhibited capacity significantly larger compared to the LCE and SBE electrode. Particularly, the PCE electrode exhibited during the second cycle a capacity about 60% higher than the SBE electrode capacity. The PCE electrode capacity gradually decreased during the following cycles until reaching the minimum value of 0.09 mAh during the 40th cycle. Following this minimum, the recorded capacity increased and then closely followed the evolution of the SBE electrode capacity during the successive 250 cycles.

In order to investigate the mechanisms responsible for the evolution of the PCE electrode capacity shown in Fig. 5B, SEM and XPS analyses of the PCE electrode were repeated at the end of galvanostatic charge-discharge cycling test. SEM images (Fig. 6) reveal random depositions (bright spots, Fig. 5B) on the electrode surface and the nanowires structure that was maintained unchanged after 250 cycles. On the other hand, as it can be seen from cross sectional SEM image (Fig. 5A), the like-solder junction [38] between the copper nanowires current collector and the PCE nanowires appears to be damaged after cycling, leading to the partial detachment of PCE nanowires. This detachment can lead to an increase in the interfacial impedance and could thus justify the fading of recorded capacity [39]. In order to ascertain the increase in the interfacial impedance, EIS was carried out at the end of galvanostatic cycling and the derived Nyquist plot was compared with that attained with the pristine electrode. The Nyquist plots attained with the PCE electrode before and after galvanostatic cycling are reported in Fig. 6A. Pristine electrode spectra can be described by the equivalent circuit model Re(RctQdl)WCin, where Re is the electrolyte resistance, Rct is the charge transfer resistance, Qdl is the constant phase element capacitance of the porous electrode, W is the Warburg diffusive element and Cin is the intercalation capacitance [40,41]. For the cycled electrode, an additional depressed semi-circular shape, which can be imputed to SEI formation, was found, and the equivalent circuit model, generally accepted at high-to-medium frequency ranges, is Re(RctQdl)(RseiQsei)WCin [39–41]. Excluding the increase in the total impedance due to the SEI, the charge transfer resistance (Rct) increased from about 30 to 60 Ω after cycling (Fig. S4, Table S2). This increase in charge transfer resistance could be imputed to the isolated active regions forming by the current collector detachment during cycling, which could thus justify the capacity fading. XPS
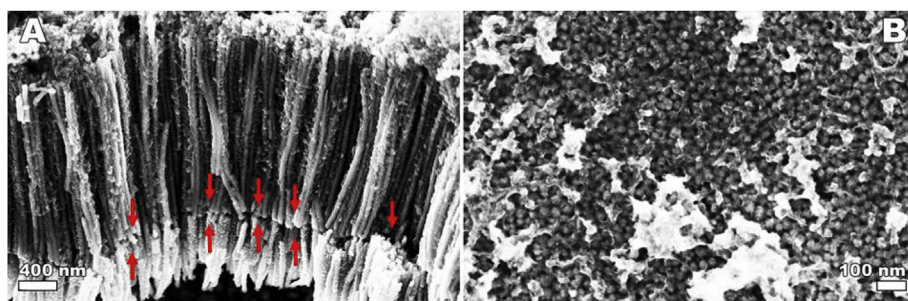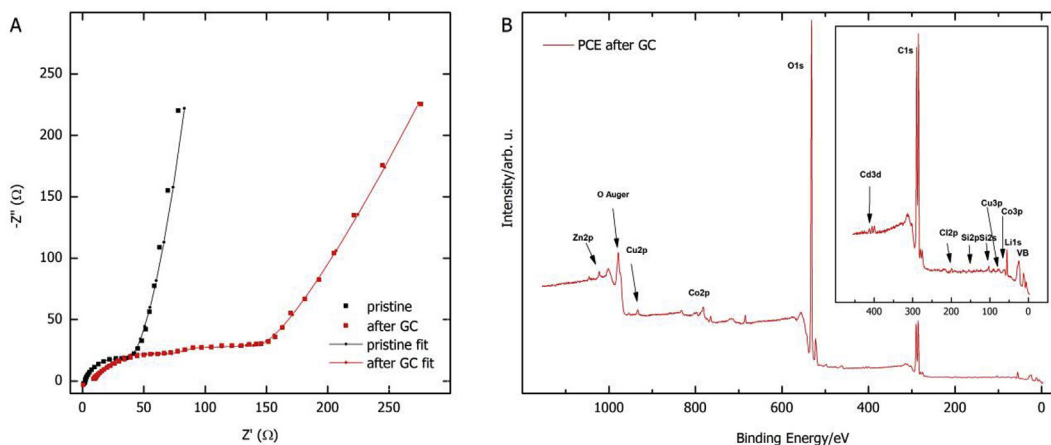

Fig. 5. A) cross sectional and top view (B) SEM images of PCE after galvanostatic cycling.

Fig. 6. A) Nyquist plot related to pristine and galvanostatically cycled PCE. B) Al Kα survey spectra of galvanostatically cycled PCE.

measurements on PCE electrode recorded after cycling have shown that the main surface contributions are given by cobalt oxide, displayed in Fig. 6B, and carbonates, as revealed by the intense C 1s peak at ~290 eV. (Fig. S5). This latter peak can be related to SEI and/or to the electrochemical driven polymerization of the electrolyte that occurs at low potential range. The presence of cobalt oxide and SEI as the prevailing components on the PCE surface justifies the close capacity trends of PCE and SBE electrodes. Indeed, the electrochemical performances of the SBE electrode are mainly determined by cobalt oxide and SEI, as discussed for the cyclic voltammetry of SBE (Fig. 4A). This is also confirmed by the similar voltage profiles obtained after 100 cycles for PCE and SBE (Fig. 4C). XPS analysis confirms that cobalt remains the relevant metallic component in PCE after electrode cycling, as apparent from the survey XPS spectra (Fig. 6B) and quantified by the relative surface atomic ratios (Table S3). On the other hand, a significant relative reduction in the amount of Cd and Ni vs. the Co amount was found on the electrode surface (Table S3). XPS of pristine PCE was characterized by a surface enrichment in CdO and NiO while Mn was found during EDX characterization. These metals oxides are characterized by a lithium storage mechanism that involves a high theoretical specific capacity [33,35,40,42]. Probably due to their dissolution into the electrolyte [43], the electroactive Cd, Ni and Mn species gradually decreased on electrode surface during cycling, justifying the capacity fading recorded during the first 40 cycles.

4. Conclusion

A new recycling process was proposed to directly produce transition metal nanowires anodes from spent LIBs. The process relies on the electrodeposition from solutions prepared using the metals recovered from the batteries electrodic powder. Two different routes were evaluated for the metals recovery, producing cobalt carbonates with different amounts of impurities, thus leading to the production of a low purity (LCE) and partially purified (PCE) anode. The performances of these anodes were benchmarked against a nanowires anode (SBE) produced by the same electrodeposition method using synthetic cobalt solution. Main conclusions of the study can be described as follows:

The LCE exhibited capacity lower than the SBE and the PCE. This can be imputed to the significantly larger copper fraction found in the LCE, which was determined by the larger copper concentration in the recovered carbonate. The mechanisms governing the charge/discharge cycling were the cobalt oxide reduction/formation and the reversible electrolyte polymerization.

The capacity of the PCE was significantly larger than that attained by the SBE and the LCE during the initial forty galvanostatic charge/discharge cycles and then it closely followed the evolution of the SBE capacity. The larger initial capacity was determined by the surface enrichment of PCE by CdO and ZnO (resulting from the contamination of the employed LIBs feedstock by different batteries types) and NiO. However, XPS analysis confirmed that such species were lost during cycling, the cobalt oxide and the electrolyte becoming eventually the only electroactive species contributing to the LCE capacity. This can explain the almost identical capacity values attained by the PCE and the SBE following the initial forty cycles.

In accordance with the illustrated study, the metal carbonate recovered after electrodic powder leaching and selective precipitation of copper can be employed as precursor to electrodeposit nanowires anodes yielding electrochemical performances similar or improved as compared the nanowires electrodeposited by using a synthetic cobalt bath. This paves the way to the simplification of the batteries recycling chain excluding the costly and lengthy separation of the different metals allowing, at the same time, to produce a high-performance batteries electrode.

References

[1] M.R. Palacín, A. de Guibert, Why do batteries fail? Science 351 (2016), 1253292.
[2] V. Etacheri, R. Marom, R. Elazari, G. Salitra, D. Aurbach, Challenges in the development of advanced Li-ion batteries: a review, Energy Environ. Sci. 4 (2011) 3243−3262.
[3] B. Scrosati, J. Hassoun, Y.-K. Sun, Lithium-ion batteries. A look into the future, Energy Environ. Sci. 4 (2011) 3287−3295.
[4] R. Schmuch, R. Wagner, G. Hörpel, T. Placke, M. Winter, Performance and cost of materials for lithium-based rechargeable automotive batteries, Nat. Energy 3 (2018) 267.
[5] B.L. Ellis, K.T. Lee, L.F. Nazar, Positive electrode materials for Li-ion and Li-batteries, Chem. Mater. 22 (2010) 691−714.
[6] H. Zou, E. Gratz, D. Apelian, Y. Wang, A novel method to recycle mixed cathode materials for lithium ion batteries, Green Chem. 15 (2013) 1183−1191.
[7] M. Agostini, A. Matic, S. Panero, F. Croce, R. Gunnella, P. Reale, S. Brutti,

A mixed mechanochemical-ceramic solid-state synthesis as simple and cost effective route to high-performance LiNi0.5Mn1.5O4 spinels, Electrochim. Acta 235 (2017) 262−269.

[8] W. Lu, X. Guo, Y. Luo, Q. Li, R. Zhu, H. Pang, Core-shell materials for advanced batteries, Chem. Eng. J. 355 (2019) 208−237.

[9] E. Gratz, Q. Sa, D. Apelian, Y. Wang, A closed loop process for recycling spent lithium ion batteries, J. Power Sources 262 (2014) 255−262.

[10] Q. Sa, E. Gratz, M. He, W. Lu, D. Apelian, Y. Wang, Synthesis of high performance LiNi1/3Mn1/3Co1/3O2 from lithium ion battery recovery stream, J. Power Sources 282 (2015) 140−145.

[11] M. Chen, Z. Zheng, Q. Wang, Y. Zhang, X. Ma, C. Shen, D. Xu, J. Liu, Y. Liu, P. Gionet, Closed loop recycling of electric vehicle batteries to enable ultra-high quality cathode powder, Sci. Rep. 9 (2019) 1654.

[12] Y. Weng, S. Xu, G. Huang, C. Jiang, Synthesis and performance of Li [(Ni1/3Co1/3Mn1/3) 1− xMgx] O2 prepared from spent lithium ion batteries, J. Hazard Mater. 246 (2013) 163−172.

[13] L. Yao, H. Yao, G. Xi, Y. Feng, Recycling and synthesis of LiNi 1/3 Co 1/3 Mn 1/3 O 2 from waste lithium ion batteries using d, l-malic acid, RSC Adv. 6 (2016) 17947−17954.

[14] L. Li, X. Zhang, R. Chen, T. Zhao, J. Lu, F. Wu, K. Amine, Synthesis and electrochemical performance of cathode material Li1. 2Co0. 13Ni0. 13Mn0. 54O2 from spent lithium-ion batteries, J. Power Sources 249 (2014) 28−34.

[15] S.H. Yu, S.H. Lee, D.J. Lee, Y.E. Sung, T. Hyeon, Conversion reaction-based oxide nanomaterials for lithium ion battery anodes, Small 12 (2016) 2146−2172.

[16] P. Li, J. Liu, Y. Wang, Y. Liu, X. Wang, K.-W. Nam, Y.-M. Kang, M. Wu, J. Qiu, Synthesis of ultrathin hollow carbon shell from petroleum asphalt for high-performance anode material in lithium-ion batteries, Chem. Eng. J. 286 (2016) 632−639.

[17] H. Luo, D. Ji, Z. Yang, Y. Huang, G. Xiong, Y. Zhu, R. Guo, Y. Wan, An ultralight and highly compressible anode for Li-ion batteries constructed from nitrogen-doped carbon enwrapped Fe3O4 nanoparticles confined in a porous 3D nitrogen-doped graphene network, Chem. Eng. J. 326 (2017) 151−161.

[18] T. Li, X. Li, Z. Wang, H. Guo, A short process for the efficient utilization of transition-metal chlorides in lithium-ion batteries: a case of Ni0. 8Co0. 1Mn0. 1O1. 1 and LiNi0. 8Co0. 1Mn0. 1O2, J. Power Sources 342 (2017) 495−503.

[19] C. Hu, J. Guo, J. Wen, Y. Peng, Preparation and electrochemical performance of nano-Co3O4 anode materials from spent Li-ion batteries for lithium-ion batteries, J. Mater. Sci. Technol. 29 (2013) 215−220.

[20] P.G. Schiavi, L. Farina, P. Altimari, M.A. Navarra, R. Zanoni, S. Panero, F. Pagnanelli, A versatile electrochemical method to synthesize Co-CoO core-shell nanowires anodes for lithium ion batteries with superior stability and rate capability, Electrochim. Acta 290 (2018) 347−355.

[21] F. Pagnanelli, E. Moscardini, P. Altimari, T. Abo Atia, L. Toro, Leaching of electrodic powders from lithium ion batteries: optimization of operating conditions and effect of physical pretreatment for waste fraction retrieval, Waste Manag. 60 (2017) 706−715.

[22] P.G. Schiavi, P. Altimari, A. Rubino, F. Pagnanelli, Electrodeposition of cobalt nanowires into alumina templates generated by one-step anodization, Electrochim. Acta 259 (2018) 711−722.

[23] M.P. Seah, D. Briggs, Practical Surface Analysis: Auger and X-Ray Photoelectron Spectroscopy, John Wiley & Sons, 1990.

[24] P.G. Schiavi, P. Altimari, R. Zanoni, F. Pagnanelli, Morphology-controlled synthesis of cobalt nanostructures by facile electrodeposition: transition from hexagonal nanoplatelets to nanoflakes, Electrochim. Acta 220 (2016) 405−416.

[25] S. Chen, S.S. Thind, A. Chen, Nanostructured materials for water splitting - state of the art and future needs: a mini-review, Electrochem. Commun. 63 (2016) 10−17.

[26] D. Briggs, Practical surface analysis, Auger X-Ray Photoelecton Spectroscory 1 (1990) 151−152.

[27] Q. Guan, J. Cheng, X. Li, B. Wang, L. Huang, F. Nie, W. Ni, Low temperature vacuum synthesis of triangular CoO nanocrystal/graphene nanosheets composites with enhanced lithium storage capacity, Sci. Rep. 5 (2015) 10017.

[28] F. Li, Q.-Q. Zou, Y.-Y. Xia, CoO-loaded graphitable carbon hollow spheres as anode materials for lithium-ion battery, J. Power Sources 177 (2008) 546−552.

[29] X. Sun, G.-P. Hao, X. Lu, L. Xi, B. Liu, W. Si, C. Ma, Q. Liu, Q. Zhang, S. Kaskel, High-defect hydrophilic carbon cuboids anchored with Co/CoO nanoparticles as highly efficient and ultra-stable lithium-ion battery anodes, J. Mater. Chem. 4 (2016) 10166−10173.

[30] K. Xie, P. Wu, Y. Zhou, Y. Ye, H. Wang, Y. Tang, Y. Zhou, T. Lu, Nitrogen-Doped carbon-wrapped porous single-crystalline CoO nanocubes for high-performance lithium storage, ACS Appl. Mater. Interfaces 6 (2014) 10602−10607.

[31] S. Grugeon, S. Laruelle, R. Herrera-Urbina, L. Dupont, P. Poizot, J. Tarascon, Particle size effects on the electrochemical performance of copper oxides toward lithium, J. Electrochem. Soc. 148 (2001) A285−A292.

[32] P. Poizot, S. Laruelle, S. Grugeon, L. Dupont, J.-M. Tarascon, From the vanadates to 3d-metal oxides negative electrodes, Ionics 6 (2000) 321−330.

[33] J. Feng, S. Xiong, Y. Qian, L. Yin, Synthesis of nanosized cadmium oxide (CdO) as a novel high capacity anode material for Lithium-ion batteries: influence of carbon nanotubes decoration and binder choice, Electrochim. Acta 129 (2014) 107−112.

[34] X.H. Huang, X.H. Xia, Y.F. Yuan, F. Zhou, Porous ZnO nanosheets grown on copper substrates as anodes for lithium ion batteries, Electrochim. Acta 56 (2011) 4960−4965.

[35] Z. Cai, L. Xu, M. Yan, C. Han, L. He, K.M. Hercule, C. Niu, Z. Yuan, W. Xu, L. Qu, K. Zhao, L. Mai, Manganese oxide/carbon yolk−shell nanorod anodes for high capacity lithium batteries, Nano Lett. 15 (2015) 738−744.

[36] L. Zhan, S. Wang, L.-X. Ding, Z. Li, H. Wang, Binder-free Co−CoO x nanowire arrays for lithium ion batteries with excellent rate capability and ultra-long cycle life, J. Mater. Chem. 3 (2015) 19711−19717.

[37] K. Cao, L. Jiao, Y. Liu, H. Liu, Y. Wang, H. Yuan, Ultra-high capacity lithium-ion batteries with hierarchical CoO nanowire clusters as binder free electrodes, Adv. Funct. Mater. 25 (2015) 1082−1089.

[38] P.-L. Taberna, S. Mitra, P. Poizot, P. Simon, J.-M. Tarascon, High rate capabilities Fe3O4-based Cu nano-architectured electrodes for lithium-ion battery applications, Nat. Mater. 5 (2006) 567−573.

[39] J.-G. Kang, Y.-D. Ko, J.-G. Park, D.-W. Kim, Origin of capacity fading in nano-sized Co(3)O(4)Electrodes: Electrochemical Impedance Spectroscopy Study, Nanoscale Res. Lett. 3 (2008) 390−394.

[40] C. Wang, D. Wang, Q. Wang, H. Chen, Fabrication and lithium storage performance of three-dimensional porous NiO as anode for lithium-ion battery, J. Power Sources 195 (2010) 7432−7437.

[41] Y.J. Mai, J.P. Tu, X.H. Xia, C.D. Gu, X.L. Wang, Co-doped NiO nanoflake arrays toward superior anode materials for lithium ion batteries, J. Power Sources 196 (2011) 6388−6393.

[42] H. Gomez, G. Riveros, D. Ramirez, R. Henriquez, R. Schrebler, R. Marotti, E. Dalchiele, Growth and characterization of ZnO nanowire arrays electrodeposited into anodic alumina templates in DMSO solution, J. Solid State Electrochem. 16 (2012) 197−204.

[43] K. Amine, J. Liu, S. Kang, I. Belharouak, Y. Hyung, D. Vissers, G. Henriksen, Improved lithium manganese oxide spinel/graphite Li-ion cells for high-power applications, J. Power Sources 129 (2004) 14−19.